PERGAMON

International Journal of Solids and Structures 36 (1999) 5573–5595

INTERNATIONAL JOURNAL OF SOLIDS and STRUCTURES

www.elsevier.com/locate/ijsolstr

Cohesive properties of nickel-alumina interfaces determined via simulation of ductile bridging experiments

R. Kolhe, S. Tang, C.-Y. Hui, A.T. Zehnder*

Department of Theoretical and Applied Mechanics, Cornell University, Ithaca, NY 14853, U.S.A.

Received 14 January 1998; in revised form 7 August 1998

Abstract

A combined experimental and computational study is carried out to characterize a nickel-alumina interface n terms of the two parameter ($\hat{\sigma}$, Γ_0) computational cohesive zone (CCZ) model of Tvergaard and Hutchnson. Experiments were performed using a sandwich specimen consisting of a thin nickel foil bonded oetween two pre-cracked alumina plates. The specimen was loaded in tension with the nickel foil bridging he cracks in the ceramic. Numerical simulations of the experiments were used to extract the parameters for he CCZ model.

Effects of various parameters of the CCZ model are investigated and it is found that the most dominant oarameter is the interface strength, $\hat{\sigma}$. Effects of the residual thermal stresses are also investigated and it is shown that these stresses can enhance the specimen fracture toughness by almost 16%. The parameters for he nickel-alumina interface are found to be $\hat{\sigma} = 148$ MPa and $\Gamma_0 = 11$ J m^{-2}. It is observed that for the foil hicknesses tested, the work of rupture does not vary linearly with the thickness as predicted by many heoretical models. We found that interfaces which are neither too strong nor too weak contribute most to he overall fracture toughness of such a composite. Although the macroscopic loading at the nickel-alumina interface is shear, the failure is primarily tensile due to the thinning that occurs in the metal as it is stretched.

1. Introduction

Composite materials consisting of a plastically deformable metal phase in a creep resistant ceramic matrix phase, have been the focus of many studies due to their potential for enhanced mechanical properties relative to those of the individual phases. When a ductile metal is combined with a brittle ceramic matrix, the resulting composite structure can retain the high yield strength of a ceramic while exhibiting an enhanced resistance to fracture, thus, making the composite a potential candidate for high performance structural applications. Optimization of these properties

* Corresponding author. Tel.: 001607 255 5062; fax: 001607 255 2011; e-mail: atz2@cornell.edu

0020-7683/99/$ - see front matter
PII: S0020-7683(98)00256-X

requires an understanding of the toughening mechanisms involved. Several toughening mechanisms such as crack shielding by ductile particles (Sigl et al., 1988), transformation toughening (Mcmeeking et al., 1982; Budiansky et al., 1983), microcrack shielding (Hutchinson, 1987) and crack-bridging (Sigl et al., 1988; Matage et al., 1989; Bao and Hui, 1989; Budiansky, 1986; Ashby et al., 1989; Bannister and Ashby, 1989) have been observed and investigated.In the composites being investigated here, i.e. Ni–Al_2O_3 system, crack bridging is the dominant mechanism of toughening (Rodeghiero et al., 1996). Several factors such as the metal–ceramic interfacial strength (Bannister and Ashby, 1991; Thurston and Zehnder, 1996), the residual thermal stresses, (Mataga, 1989; Kolhe et al., 1996), the degree of the metal ductility (Bao and Hi, 1989) and the morphology, size and volume fraction of the inclusions (Budiansky, 1986) influence the crack bridging mechanism.

A number of researchers have analyzed and modeled the crack bridging mechanism. In these studies, models are proposed to estimate the enhancement in fracture toughness of a composite for crack extension under steady state conditions. In general, the enhancement in fracture toughness is estimated by establishing a relationship between separation of the crack faces and the average stress supported across the crack faces by the bridging inclusions. The fracture toughness enhancement can be written as

$$\Delta G \approx f\sigma_Y h \int_0^{U_c/h} \frac{\sigma}{\sigma_Y} \mathrm{d}\left(\frac{u}{h}\right), \tag{1}$$

where σ is the nominal stress supported across the crack faces, u is the crack face separation, U_c is the value of u at failure of the inclusion, f is the area fraction of the inclusions intercepted by the crack, and h is a length measure of the size of inclusion. Sigl et al. (1988) have estimated relationship between σ/σ_Y and u/h using the Bridgman solution for the mean axial stress is cylindrical bars. Bao and Hui (1989) extended the analysis of Sigl et al. (1988) by incorporating a pre-existing interfacial debond length. Mataga (1989) carried out calculations of constrained necking to establish the relation between the nominal stresses in the inclusion and the crack face separation. None of these studies explicitly accounts for the interfacial behavior between the inclusion and the matrix.

Ashby et al. (1989) and Bannister and Ashby (1991) carried out experiments to study the effect of interface debonding on fracture toughness. These studies revealed the important role of the interfacial strength in controlling the fracture toughness. Their analytical models, however, are too simple to capture all the relevant mechanics. The difficulty in accounting for the interfacial strength in analytical models lies in the quantitative characterization of interfaces and modeling of the debond crack growth. Despite continuous efforts to understand the mechanics of interface fracture, there is still controversy surrounding the interface crack tip field in a bimaterial with at least one elasto-plastic component. For example, there is no consensus on the usage of singular fields to characterize the fracture behavior of such interface. Indeed, the recent studies of Sharma and Aravas (1993) and Bose and Ponte Castaneda (1992) on the interfaces between a ductile solid and an elastic solid indicate that for some geometries and some loadings, the region of dominance of these crack tip singular fields is so small that it does not have any physical relevance. In such cases, the characterization of interface in terms of singularity based fracture mechanics approach is questionable.

In this study, the computational cohesive zone model (CCZ model) based on a cohesive zone

concept (Barenblatt, 1962; Dugdale, 1960) is used to characterize the nickel–alumina interface and to simulate the debond crack growth. Within the frame-work of the CCZ model, the mechanical response of the interface is primarily specified by the interfacial strength, $\hat{\sigma}$, and work of separation per unit area, Γ_0. The CCZ model was first proposed by inclusion variations (Allen et al., 1994; Tvergaard and Hutchinson, 1992, 1993, 1994a, 1994b, 1996a, 1996b). Tvergaard and Hutchinson have demonstrated that the CCZ model can reproduce established fracture mechanics results. In all of the above studies, the values for the parameters, the work of separation per unit area and the interface strength, are assumed a priori or are varied to perform parametric studies. In this study, we obtain these parameters for a nickel–alumina interface using a combined experimental–computational approach. The experiment reported here was designed to investigate the strength of the Ni–Al_2O_3 interface and to gain insight into the toughening mechanism for cracks bridged by platelet-shaped metal inclusions. A computer simulation is carried out to determine the interface behavior by iterating the parameters in the CCZ model until the predicted and measured load displacement data agree. The computer simulation also allows us to investigate effects of the stresses and size of inclusions on the toughness.

2. Experimental procedures

The experiment is similar to those performed by Ashby et al. (1989). The sample geometry consisted of a layer of 99.9% pure nickel foil bonded between two 99.9% alumina plates as shown in Fig. 1. The specimens were prepared by hot-pressing under reducing conditions in a controlled atmosphere furnace at 1300°C for 2 h. The atmosphere at the bonding temperature was set by controlling the CO/CO_2 ratio so that the log of oxygen partial pressure was -10.54; well below the threshold of creating spinel and other Ni–Al–O compounds. After bonding, pre-cracks in both alumina plates were obtained by first making indentations along the sample's centerline and then loading the specimen in three point bending until a crack popped in. Some debonding was observed along the interface. The initial debond length was for one specimen measured using the dye

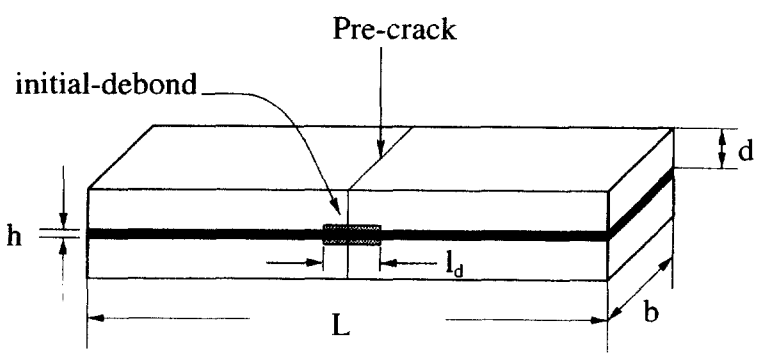

Fig. 1. Specimen geometry: $L = 20$ mm; $b = 5$ mm; $d = 2$ mm, $l_d = 0.23$ mm. Two foil thickness, $h = 125$ μm and $h = 250$ μm were used.

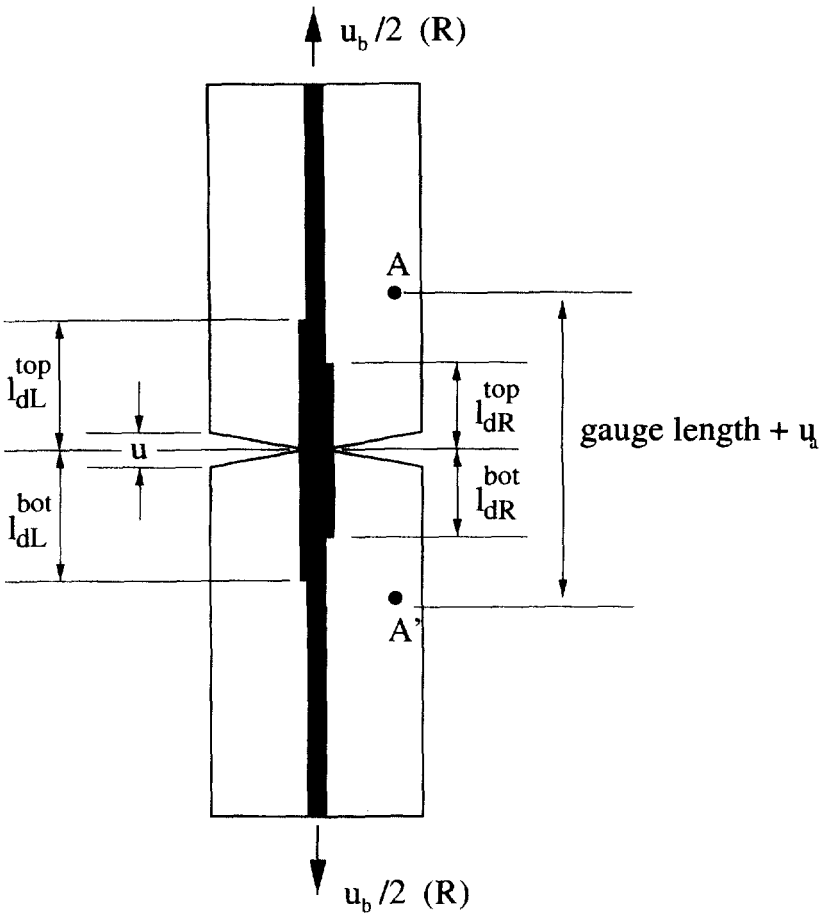

Fig. 2. Schematic diagram of the experimental set-up: u is the separation of the pre-crack surfaces at the edge of the specimen, u_a is the displacement recorded by the extensometer, and u_b is the load point displacement. The reaction force exerted on the specimen is denoted by R.

penetrant method. This length was used as the initial-debond length in the numerical simulations.

The pre-cracked specimen, (Fig. 2) was loaded in tension with a universal testing machine. An extensometer with a 5 mm gage length (between points A and A′ in fig. 2) was used to record the crack opening displacement. Let u be the separation of the pre-crack surfaces at the edge of the specimen (see Fig. 2), u_a be the displacement recorded by the extensometer, and u_b be the load point displacement. Since the ceramic is elastic, and much stiffer than the plastically deforming thin metal foil $u \approx u_a \approx u_b$. After each test, the final debond length was measured using dye penetrants. The reaction force-displacement curve was recorded directly in a computer. To extract the interface properties in terms of the CCZ model, the experiment was then simulated using the finite element method and the CCZ parameters iterated until the computed and measured load displacement results agreed.

3. Computational cohesive zone model

In the framework of the computational cohesive zone model, the interface is characterized by a traction separation law that gives the rupture energy and strength of the interface. The traction separation law can in this case be thought of as a continuum model of the detailed failure processes occurring in the 'fracture process zone' ahead of the crack tip. Figure 3 depicts a fracture process zone modeled by the traction separation law. The normal and shear tractions are indicated by t_n and t_t, respectively, and Δu_n and Δu_t are the normal and shear components of the relative displacement of the crack faces across the interface, respectively. The normal and tangential components of the traction acting on the interface are given by

$$t_n = \frac{\sigma(\lambda)}{\lambda}\frac{\Delta u_n}{\delta_n} \tag{2}$$

$$t_t = \frac{\sigma(\lambda)}{\lambda}\frac{\delta_n}{\delta_t}\frac{\Delta u_t}{\delta_t}, \tag{3}$$

where

$$\lambda = \sqrt{(\Delta u_n/\delta_n)^2 + (\Delta u_t/\delta_t)^2}, \tag{4}$$

is a non-dimensional separation measure, δ_n and δ_t are critical values of the displacements Δu_n, and Δu_t respectively, and the function $\sigma(\lambda)$ is a function of λ as depicted in Fig. 4. The parameters λ_1 and λ_2 determine the shape of the function $\sigma(\lambda)$. The interface decohesion is modeled in terms of an interface potential that specifies the dependence of the traction t_n and t_t on the normal and tangential components, Δu_n and Δu_t, of the relative displacement of the crack faces across the

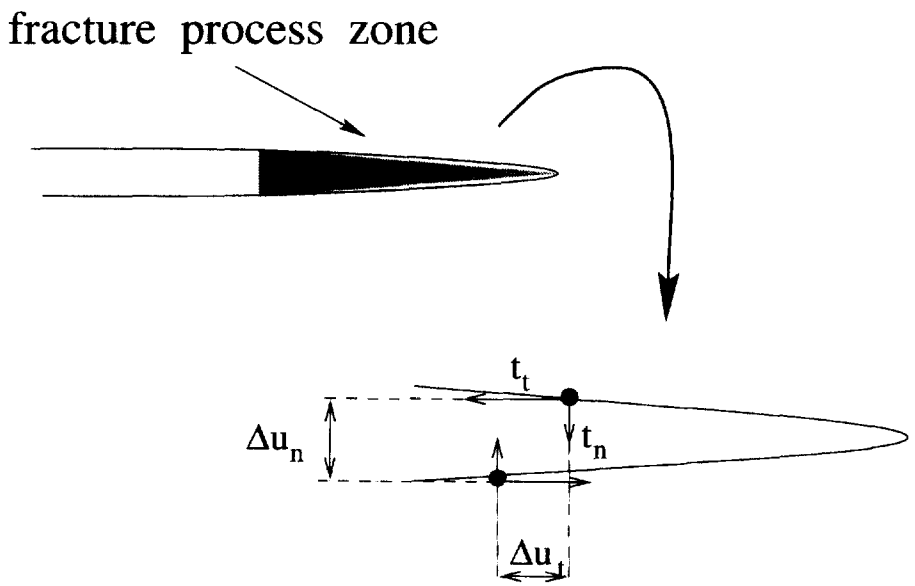

Fig. 3. Fracture process zone.

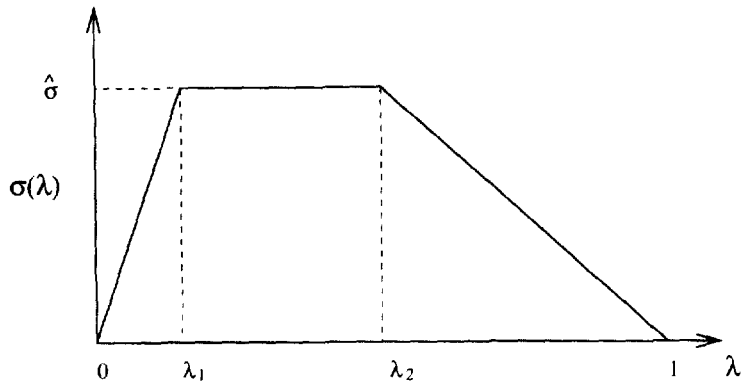

Fig. 4. Interface traction separation law.

interface. In purely normal separation ($\Delta u_t = 0$), the traction law is $t_n = \sigma(\lambda)$ and total separation occurs at $\Delta u_n = \delta_n$. In purely tangential displacement ($\Delta u_n = 0$), the traction law is $t_t = \sigma(\lambda)(\delta_n/\delta_t)$ and total separation occurs when $\Delta u_t = \delta_t$. The peak normal traction under pure normal separation is $\hat{\sigma}$, and the peak shear traction is $(\delta_n/\delta_t)\hat{\sigma}$ in a pure tangential separation. The traction separation law listed in eqn (2) can be derived from the potential

$$\Phi(\Delta u_n, \Delta u_t) = \delta_n \int_0^{\lambda} \sigma(\lambda')\, d\lambda'. \tag{5}$$

The work of separation in the process zone is

$$\Gamma_0 = \tfrac{1}{2}\hat{\sigma}\delta_n(1-\lambda_1+\lambda_2). \tag{6}$$

The parameters governing the separation law are, therefore, the work, Γ_0, of the fracture process, the peak normal traction, $\hat{\sigma}$, $\hat{\sigma}$, the critical displacement ratio δ_n/δ_t, and the shape parameters λ_1 and λ_2. The values of λ_1, λ_2 and δ_n/δ_t are fixed in this study. They are chosen to be 0.15, 0.50 and 1.0, respectively. In this way, the number of parameters to be extracted is reduced to two.

4. Material properties

In the present study a rate independent elastic-plastic material model based on J_2 flow theory is used for the metal layer of nickel. Uniaxial stress–strain curves for nickel at different temperatures ranging from 304 to 1090 K have been tabulated by Thurston (1994). The room temperature value of the yield stress is 82 MPa and will be denoted by σ_Y. Thurston has found the strain hardening coefficient at room temperature to be 3.13. Young's modulus and Poisson's ratio of nickel are also considered as a function of temperature. The room temperature values of Young's modulus and Poisson's ratio of nickel are 208 GPa and 0.312, respectively. The coefficient of thermal expansion, α, of nickel is assumed to be constant and equal to $15.5 \times 10^{-6}\ K^{-1}$. Alumina is assumed to be linearly elastic throughout the analysis. The properties E, ν and α of alumina are assumed to be independent of temperature and equal to 390 GPa, 0.245 and $7.4 \times 10^{-6}\ K^{-1}$, respectively.

5. Numerical procedure

The model experiment is simulated using a quarter geometry specimen and symmetric boundary conditions as shown in Fig. 5. Note that Fig. 5 is not drawn to scale. The interface between the ceramic and nickel was modeled using the interface elements described in the Appendix and the continuum was discretized using four noded quadrilateral elements. A uniform mesh was used in the region of length $H_0 = 15\ h$ ahead of the initial debond crack tip. Let Δ_0 be the length of an interface element, then $H_0 = 600\ \Delta_0$ for the finer mesh and $H_0 = 300\ \Delta_0$ for the coarser mesh. The thickness of the metal layer is $h = 125\ \mu$m. For the thick specimens, $h = 250\ \mu$m. The finer mesh consists of 24 quadrilateral elements across the metal layer. Sixteen elements are used in the coarse mesh.

Computations were performed for the case of plane strain with an assumption that far from the edges the three dimensional stress state is similar to that of the plane strain. The plane strain assumption is well satisfied by the experimental set-up until the interface crack length is comparable to the out-of-plane dimensions of the specimen. ABAQUS software with a user subroutine for the interface elements was used for these computations. Details of the interface element are given in the Appendix. Integration over the interface elements was done using three point Gauss rule. The analysis of the specimen was done in three steps.

In the first step, residual thermal stresses are calculated. The rate independent elastic-plastic material model described earlier is used for the metal. The actual cooling is slow, so that a spatially uniform temperature field can be assumed at each time to compute the residual stresses. A transient

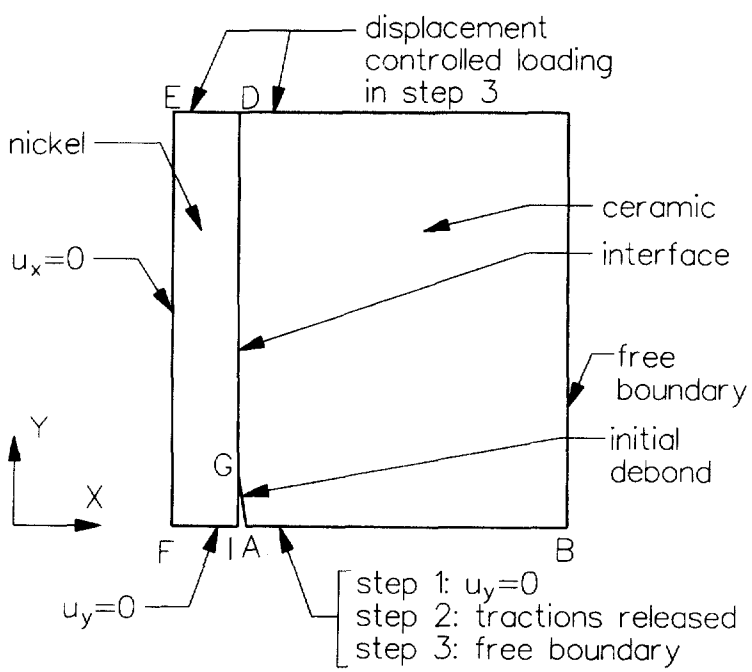

Fig. 5. Schematic of the quarter specimen geometry and the boundary conditions (not to scale).

heat conduction analysis coupled with stress analysis may result in a slightly different residual stress field after cooling. At a high temperature, just after processing, the material is taken to be stress free; but stresses build up during cooling to room temperature, due to thermal expansion mismatch between the metal and the ceramic. The material properties $\sigma_y(T)$, $E(T)$ and $\nu(T)$ are assumed to be temperature dependent.

In the second step, a crack is introduced in the ceramic by releasing the nodal reaction forces at the degrees of freedom restrained along the boundary AB (see Fig. 5).

In the third step, the specimen is loaded in displacement control in the axial direction (y-direction in Fig. 5). The analysis is stopped once the axial load levels off.

Recall, in the experiments, the initial debond (AG in Fig. 5) is introduced during pre-cracking of the specimen (i.e., during step 2). However, for computational simplicity, this initial debond is assumed to exist during processing (i.e., step 1). To check the validity of this assumption, we also carried out the residual stress calculations with a perfectly bonded interface. The difference in the calculated residual stress fields for the two cases was very small.

6. Results and discussion

6.1. Experimental results

Figures 6 and 7 show experimentally obtained plots of averaged nominal stress in the metal strip vs the crack opening displacement for the specimens with metal layer thickness 125 and 250 μm,

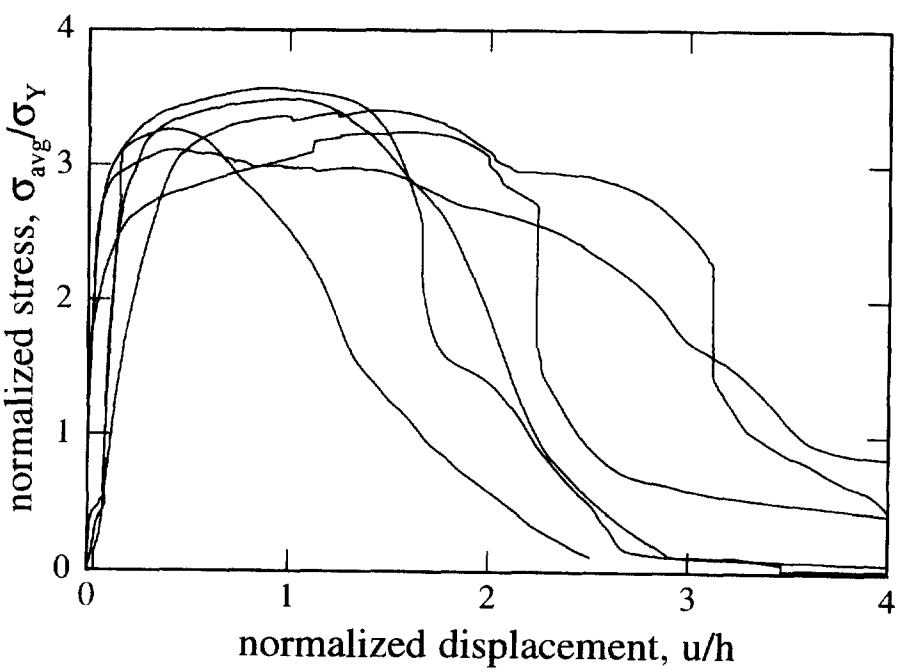

Fig. 6. Average nominal stress in the metal strip vs (h = 125 μm) crack opening displacement for six nominally identical specimens.

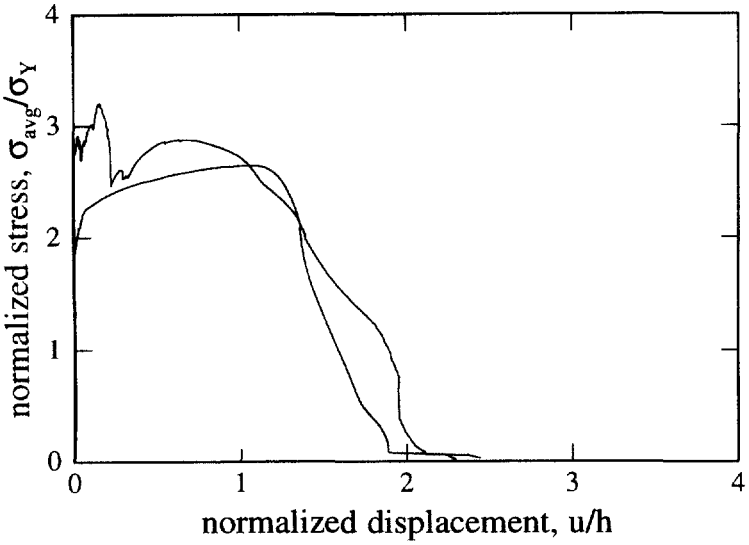

Fig. 7. Averaged nominal stress in the thick ($h = 250$ μm) metal strip vs crack opening displacement for two nominally identical specimens.

respectively. During loading, the crack faces separate and stresses build up in the metal strip. The nominal tensile stress, σ_{avg}, in the metal strip is calculated by dividing the recorded reaction force, R, by the initial area of the metal strip. Initially, the nominal stress increases monotonically with the displacement, then reaches a plateau and finally, it drops to zero as the specimen necks. The peak stress level, σ_{max}, achieved is approximately $3.2 \pm 0.2\ \sigma_Y$. It was observed that the final debond lengths, i.e. l_{dL}^{top}, l_{dL}^{bot}, l_{dR}^{top}, l_{dR}^{bot} (see Fig. 2) varied from specimen to specimen, but were in the range of 0.4–1.0 mm. Also, it was observed that the debonding was not always symmetric, i.e. $l_{dL}^{top} \neq l_{dR}^{top}$ and $l_{dL}^{bot} \neq l_{dR}^{bot}$. Figure 6 shows that there is considerable test to test variation in the magnitude of the crack opening displacement at which the nickel foil starts to neck.

The work done, W_r, in fracturing the nickel layer, per unit cross sectional area, is approximated by

$$W_r \approx \frac{1}{bh}\int_0^{U_c} R\,du, \tag{7}$$

where R is the reaction force, u is the crack opening displacement at the edge of the specimen and U_c is the crack opening displacement when the necking starts (Note, $u_b \sim u$ as mentioned earlier). The above equation can be written in terms of normalized variables as

$$W_r \approx \sigma_Y h \int_0^{U^*} \chi\,du^*, \tag{8}$$

where $U^* = U_c/h$, and $\chi = \sigma/\sigma_Y$. Integrating the experimental data for six samples and taking the average yields $W_r \approx 7.6 \pm 1.4\ \sigma_Y h$. For the thick specimens, $W_r \approx 4.2 \pm 0.5\ \sigma_Y h$. It is interesting to note that, at these foil thicknesses, the work of rupture per unit area is not linearly proportional

to the thickness of the layer as proposed by Bannister and Ashby (1991). In other words, the constant of proportionality is a function of h. Figures 6 and 7 indicate that as the thickness of the metal layer increases, the average nominal stress decreases. The computational model also predicts a similar trend. Budiansky (1986) and others (Sigl et al., 1988; Tuan and Broom, 1990) have assumed that the nominal stress does not vary with the size of an inclusion and have proposed that the work of rupture is linearly proportional to the size of an inclusion. Our results indicate that this is not the case, at least when there is some debonding of the interface.

6.2. Computational results

At the end of step 1, the thermal residual stress σ_{yy} parallel to the interface, is essentially constant in the metal strip and is equal to $1.2\,\sigma_Y$. Away from the crack the stresses σ_{zz} and σ_{xy} are negligible, therefore, away from the crack the nickel is in biaxial tension. At the end of step 2 (unloading to create the crack) the cracks will interpenetrate. During loading, step 3, this interpenetration is reversed and the foil is reloaded in tension. The progression of deformation of the metal during step 3 (axial tensile loading) is shown in Fig. 8.

Figure 9 plots computed average normalized stress as a function of the normalized crack opening displacement for different values of the interface parameter, $\hat{\sigma}$. For these plots, $\hat{\sigma}$ is varied and δ_n and δ_t are kept constant. For $\hat{\sigma}/\sigma_Y \geqslant 6.0$, the computations indicate that debonding along the interface does not take place and the nickel foil necks with little stretching. In fact, we find that for $\hat{\sigma}/\sigma_Y > 6.0$, curves of the average normalized stress vs the normalized crack opening displacement are practically identical to the curve for $\hat{\sigma}/\sigma_Y = 6.0$. For $\hat{\sigma}/\sigma_Y \leqslant 5.0$, the average nominal

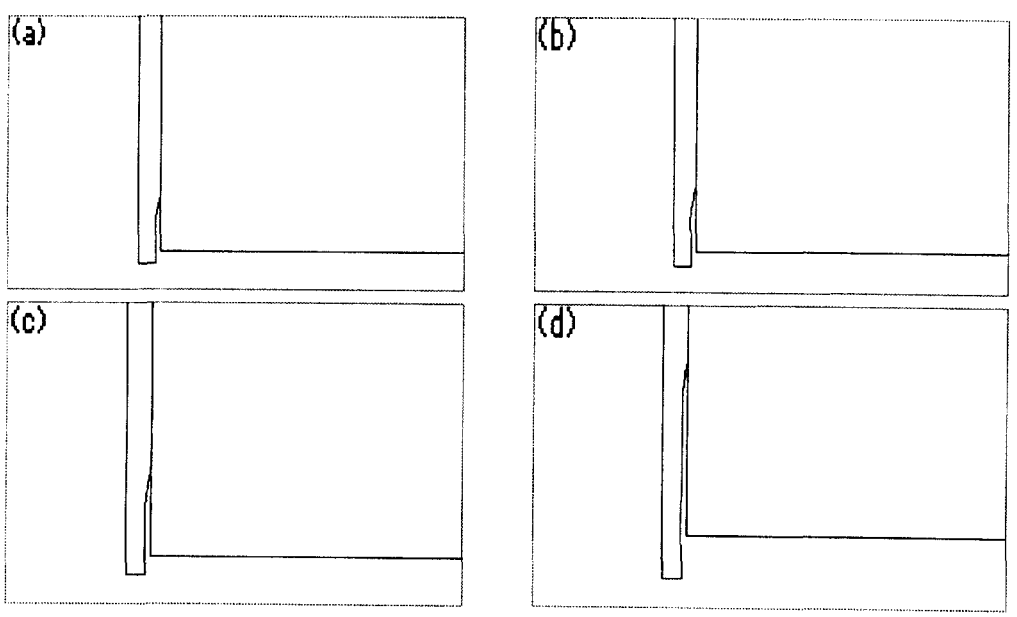

Fig. 8. Progressive stages of deformation of the metal strip and the interface debond crack.

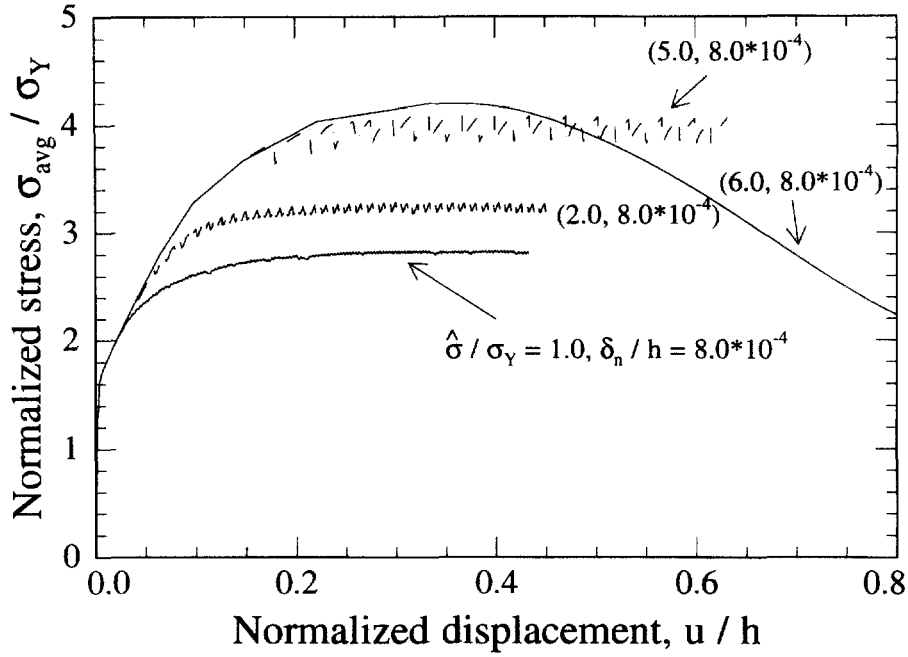

Fig. 9. Plots of normalized stress vs normalized crack opening displacement for different values of the interface parameters. For $\hat{\sigma}/\sigma_Y \leqslant 5$, the debond crack propagates at steady state whereas for $\hat{\sigma}/\sigma_Y \geqslant 6$, the debond crack does not grow and metal fails by necking.

stress reaches a maximum and then levels off, indicating that the debond crack grows steadily. In this range of $\hat{\sigma}$ values, the computed average maximum nominal stress, σ_{max}, increases as $\hat{\sigma}$ increases.

Although we have not continued the computations until the metal strip fails, a reasonable estimate of the work of rupture can be found out by assuming $U^* = 2.0$ (approximate experimentally observed value of the crack opening displacement at the time of rupture) for the curves plotted for $\hat{\sigma}/\sigma_Y \leqslant 5.0$. The work of rupture for $\hat{\sigma}/\sigma_Y \geqslant 6.0$ is calculated using $U^* = 1.0$, since according to our simulations (Fig. 9) necking is expected to be complete at this value of the crack opening displacement. The work of rupture, W_r, is computed to be 5.6 $\sigma_Y h$, 6.4 $\sigma_Y h$, 7.8 $\sigma_Y h$ and 4.1 $\sigma_Y h$ for $\hat{\sigma}/\sigma_Y = 1.0$, 2.0, 5.0 and 6.0, respectively. The maximum work of rupture is more for $\hat{\sigma} = 5.0\ \sigma_Y$ than for $\hat{\sigma} = 6.0\ \sigma_Y$. These calculations confirm the notion that the maximum work of stretching is achieved for an interface which is neither too strong nor too weak.

Figure 10 demonstrates the effect of $\hat{\sigma}$ (for constant δ_n) on the average maximum nominal stress in the metal strip. As $\hat{\sigma}$ increases, the average maximum nominal stress increases. It can also be seen from Fig. 10 that for the specimen with twice the metal strip thickness, the nominal stress levels are lower than the thinner strip specimen. This is most likely due to the loss of constraint in the middle of the layer with higher thickness. Figure 11 demonstrates the effect of the interface displacement parameter, δ_n, on the average maximum nominal stress in the metal strip. The average maximum nominal stress increases slightly as δ_n increases.

The effects of various other interface parameters on the average nominal stress vs crack opening displacement curve were also investigated. It was observed that the effect of the parameters such

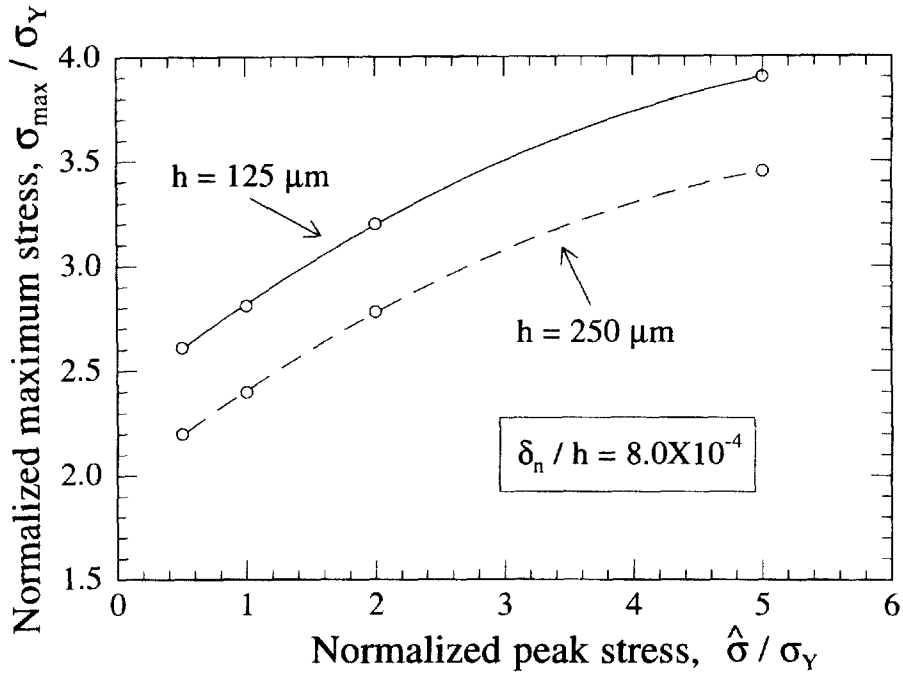

Fig. 10. Effect of the peak traction, $\hat{\sigma}$, on the average maximum nominal stress in the metal strip.

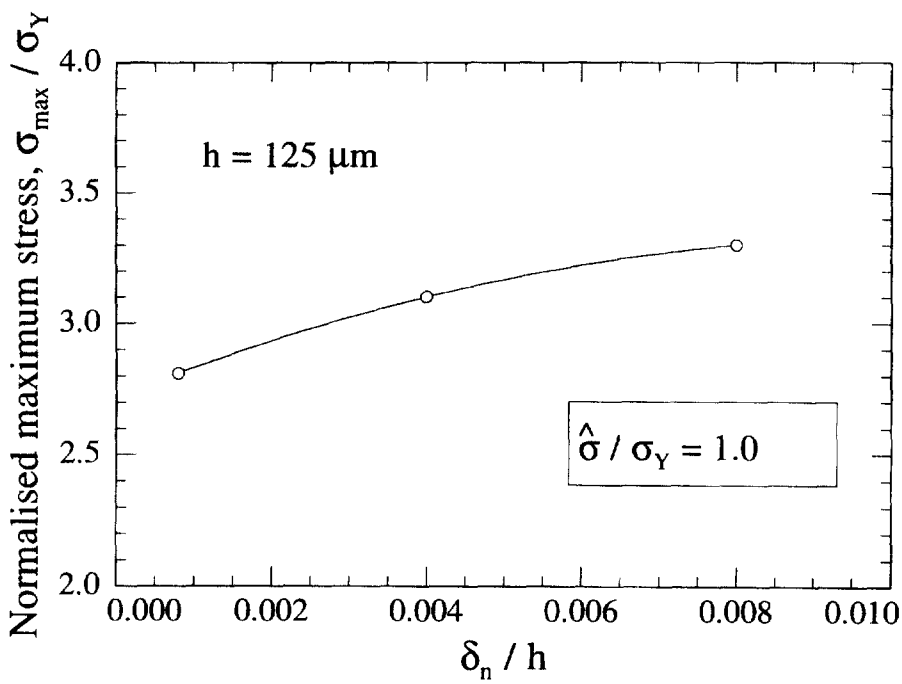

Fig. 11. Effect of δ_n on the average maximum nominal stress in the metal strip.

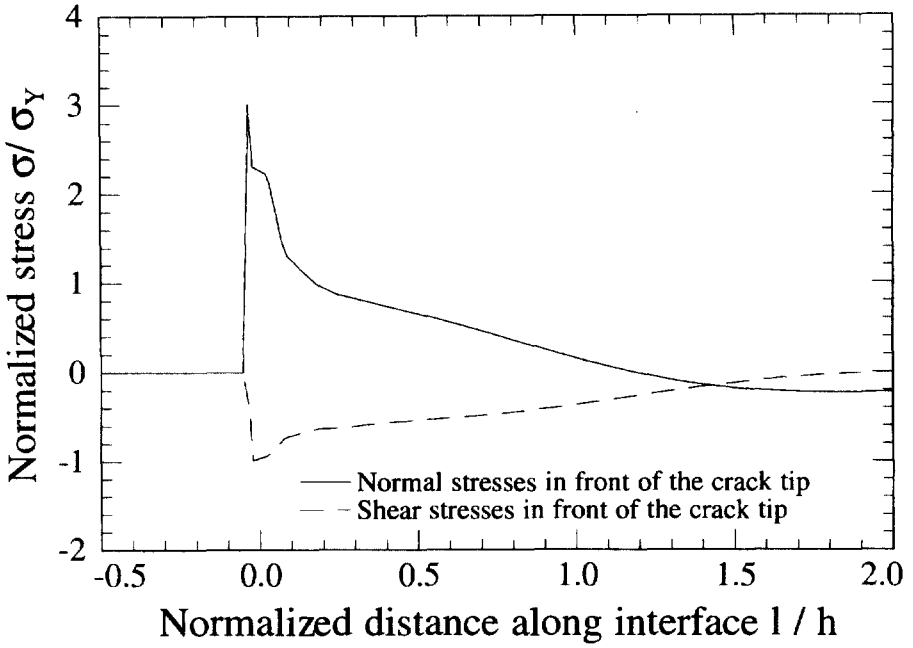

Fig. 12. A plot normalized traction in the fracture process zone in front of the crack tip for the specimen with interface parameters of $\hat{\sigma}/\sigma_Y = 5.0$; $\delta_n/h = 0.0008$.

as the ratio of maximum normal to shear separation, i.e. δ_n/δ_t, the shape parameters, λ_1 and λ_2, and the initial debond length, l_d are very small. Lowering the ratio of δ_n/δ_t to 0.2 slightly lowered the level of average nominal stress. Changing the initial debond length had no effect on the maximum level of the stresses reached, but the initial slope of the curve of nominal stress vs displacement was altered slightly. It can be concluded from these plots that effects of these parameters are secondary. This is also observed by Tvergaard and Hutchinson.

Figures 12 and 13 show tractions in the process zone in front of the debond crack tip. Note that the magnitude of the maximum normal traction is sometimes (Fig. 12) almost three times that of the maximum shear traction. It is interesting to note that, even though the interface is macroscopically loaded in shear, the ratio of normal to the shear separation was found to be 3/2. For the case of $\hat{\sigma}/\sigma_Y = 1.0$; $\delta_n/h = 0.008$, this ratio was as high as 4.0. Recall that the metal is under plane-strain constraint, thus the strain in the z-direction is zero. To accommodate the tensile stretching in the y-direction the material must contract in the x-direction. Thus the interfacial failure, is in the end dominated by tension stresses.

6.3. Determination of the interface parameters

The interface parameters, $\hat{\sigma}$ and δ_n, were determined by comparing the computed plots with the experimental plots. The computed plots for different values of the interface parameters are shown in Fig. 9. Figures 14 and 15 both show the curve of the computed average normalized stress vs the normalized crack opening displacement and the curve of the experimentally recorded average

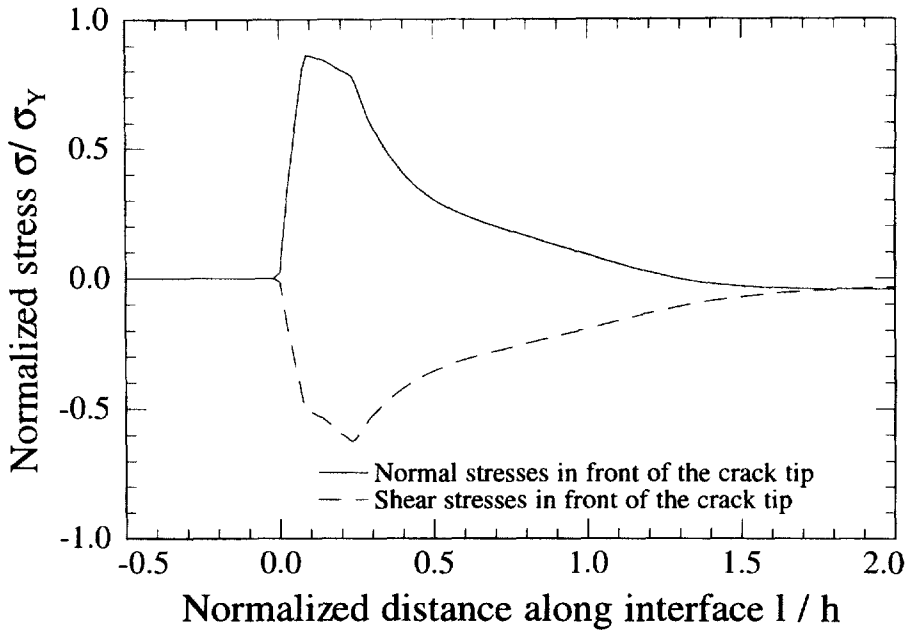

Fig. 13. A plot normalized traction in the fracture process zone in front of the crack tip for the specimen with interface parameters of $\hat{\sigma}/\sigma_Y = 1.0$; $\delta_n/h = 0.008$.

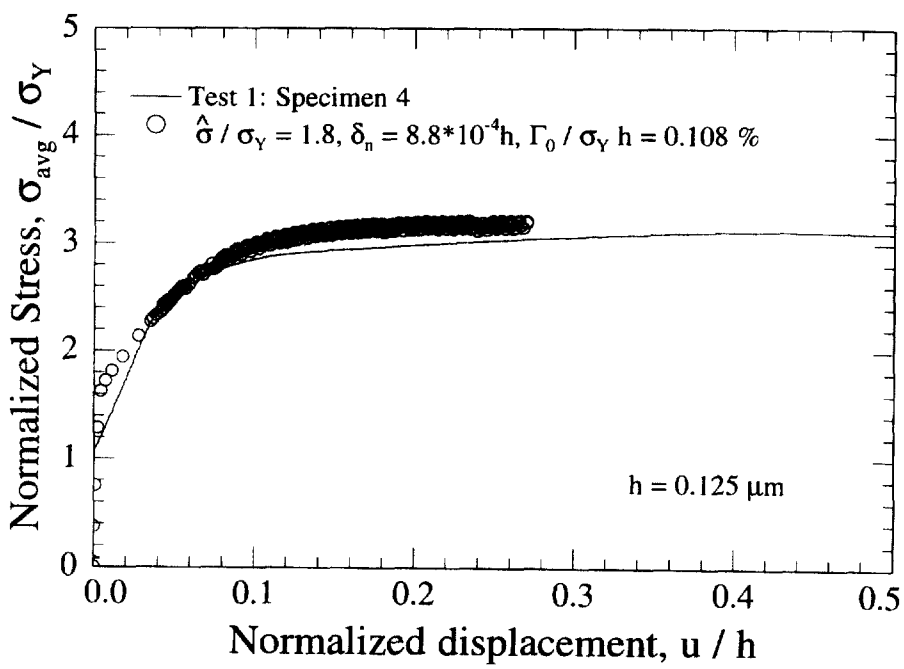

Fig. 14. The computed plot for the thick specimen with the interface parameters $\hat{\sigma} = 1.8\ \sigma_Y$ and $\delta_n = 8.8 \times 10^{-4}\ h$, i.e., $\Gamma_0/\sigma_y h = 0.108\%$ and the experimental plot for specimen 4.

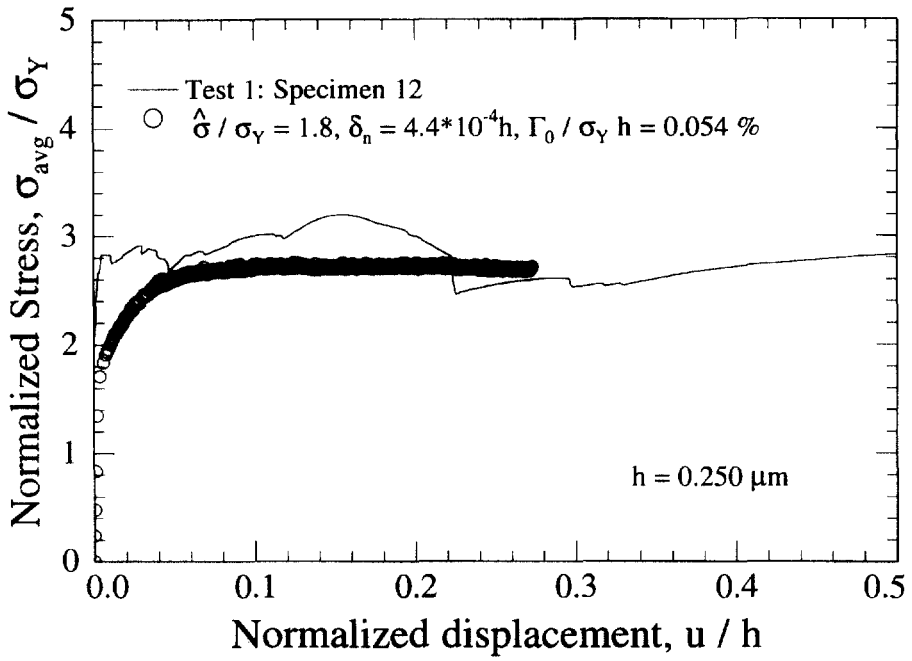

Fig. 15. The computed plot for the thick specimen with the interface parameters $\hat{\sigma} = 1.8\ \sigma_Y$ and $\delta_n = 4.4 \times 10^{-4}\ h$, i.e., $\Gamma_0/\sigma_y h = 0.054\%$ and the experimental data for specimen 12.

normalized stress vs the crack opening displacement for the specimens with $h = 0.125$ μm and $h = 0.250$ μm, respectively. The computed curves are plotted using the same parameters for the thick and thin foil, $\hat{\sigma} = 1.8\ \sigma_Y$ and $\delta_n = 8.8 \times 10^{-4}\ h$, where here, h refers to the 125 μm thickness of the thin foil.

Figure 16 shows plot of the computed debond-crack length vs the normalized crack opening displacement. The slope of the debond crack length vs the crack opening displacement is constant (Fig. 16), indicating steady debond crack growth. Linear extrapolation of these results would predict a final debond crack length of $18h$ for the crack opening displacement of $2h$ (average of the observed crack opening displacement at the time of rupture in the experiments). This is in the range of the measured final debond-crack lengths of $8h$ to $20h$. It should be noted that the computations are done for a symmetrically debonded specimen, i.e., $l_{dL}^{top} = l_{dL}^{bot} = l_{dR}^{top} = l_{dR}^{bot}$, whereas in the experiments it was not possible to grow the debond cracks symmetrically. It has been pointed out by Bannister and Ashby (1991), that in the case of asymmetric debonding, plastic deformation is intensified and is confined to a thin band. This may also affect the debond crack growth. Asymmetric debonding could also be the reason for the large variation observed in the crack opening displacement at rupture (1.2–3.2h).

6.4. *Effect of residual stresses*

Our calculations demonstrate that the initial debond crack does not grow during step 1, leading us to conclude that flaws along the interfaces between nickel platelets and alumina matrix would not grow during processing of the composite.

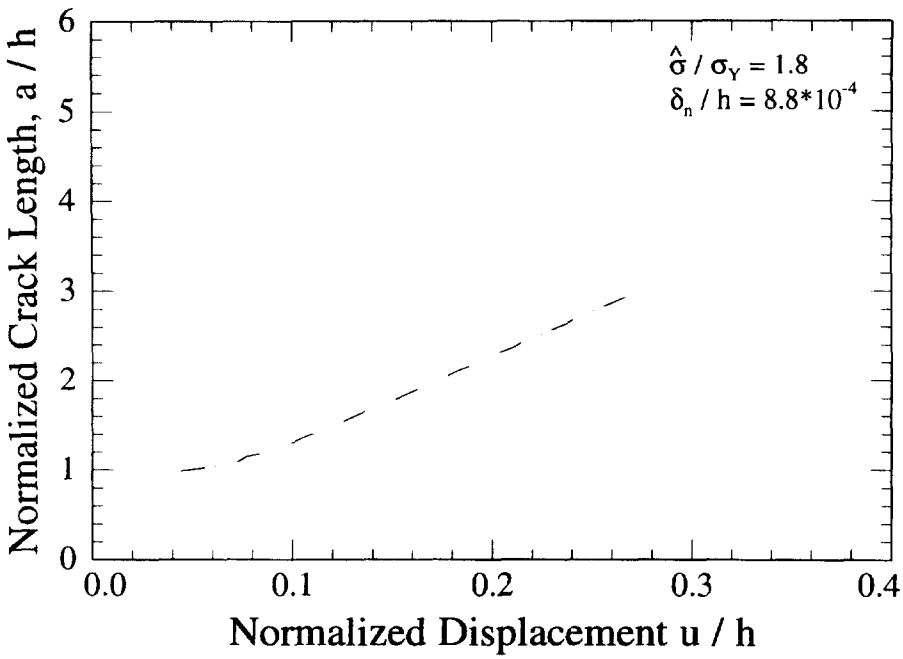

Fig. 16. Plots of normalized debond crack length vs normalized crack opening displacement for different values of the interface parameters.

Figures 17 and 18 show plots of the computed normalized average nominal stress in the metal layer vs the normalized crack opening displacement for two different interface laws. The debonding behavior for Figs 17 and 18 is taken to be described by the sets of parameter values $\hat{\sigma} = 1.0\ \sigma_Y$, $\Gamma_0/\sigma_Y h = 0.54\%$ and $\hat{\sigma} = 1.8\ \sigma_Y$, $\Gamma_0/\sigma_Y h = 1.08\%$, respectively. The figures show two plots, the dotted line represents a plot in absence of the residual stress and the solid line shows the one with the residual stresses. The residual thermal stresses parallel to the interface were computed to be of the magnitude $1.2\ \delta_Y$ in the metal layer. In the computations, no interface debonding was observed during the cooling stage. The magnitude of the residual thermal stress parallel to the interface in the thick specimen was also calculated to be $1.2\ \sigma_Y$. Using a rate-dependent model and performing a transient analysis, Thurston and Zehnder (1996) report values of the residual stresses around $1.4\ \sigma_Y$ for a similar geometry.

Figure 17 shows that if residual stresses were included in the analysis σ_{max}/σ_Y is equal to 3.3, whereas for the plot without considering residual stresses, σ_{max}/σ_Y is 2.1. Assuming U^* to be the same for both the plots and equal to the experimentally observed value of 2.0, the work of rupture is $6.6\ \sigma_Y h$ and $4.2\ \sigma_Y h$ for the cases with and without considering residual stresses, respectively, i.e., the value of the work of rupture in the calculation considering residual stresses is 1.6 times higher than the one without considering residual stresses. The same is true for a different set of interface parameters as shown in Fig. 18. In this case the increase in the work of rupture is 1.3 times higher. This observation agrees with the results of Bao and Hui (1989) and Mataga (1989).

Our computations show that σ_{max} is considerably higher for the calculations considering residual

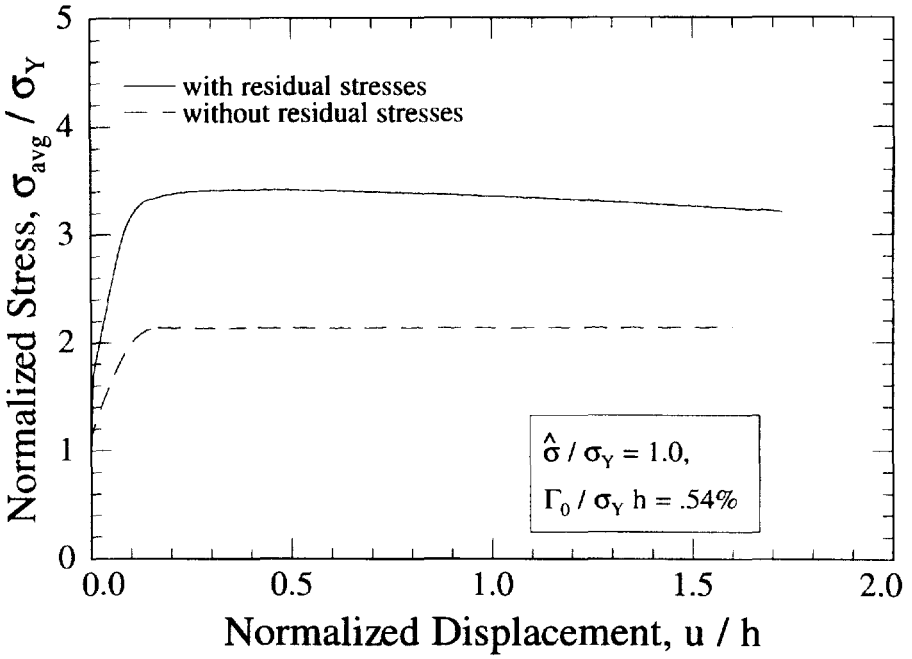

Fig. 17. Effect of residual stresses on the load displacement curve.

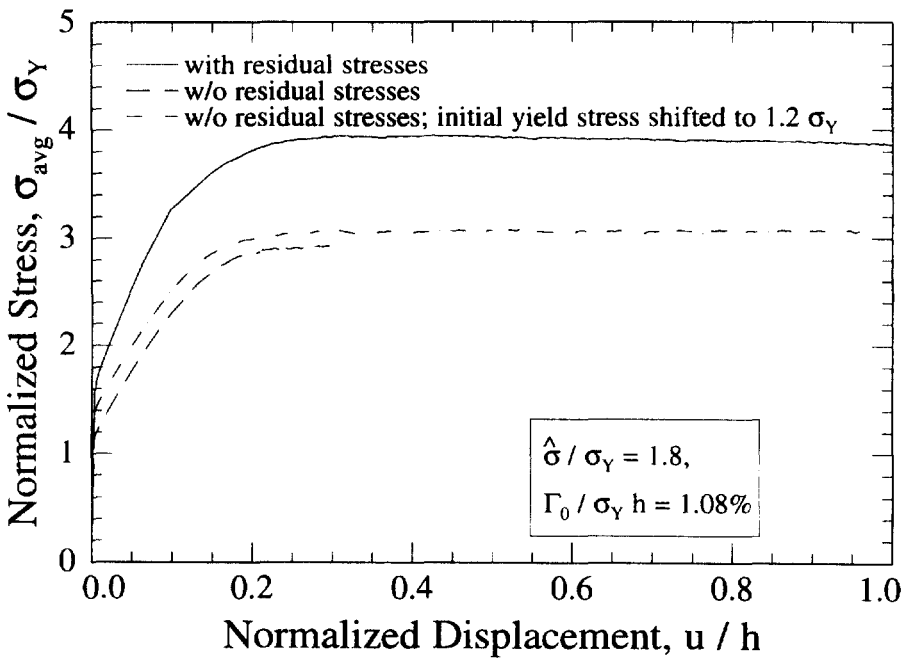

Fig. 18. Effect of residual stresses and the initial yield stress at the room temperature on the load displacement curve.

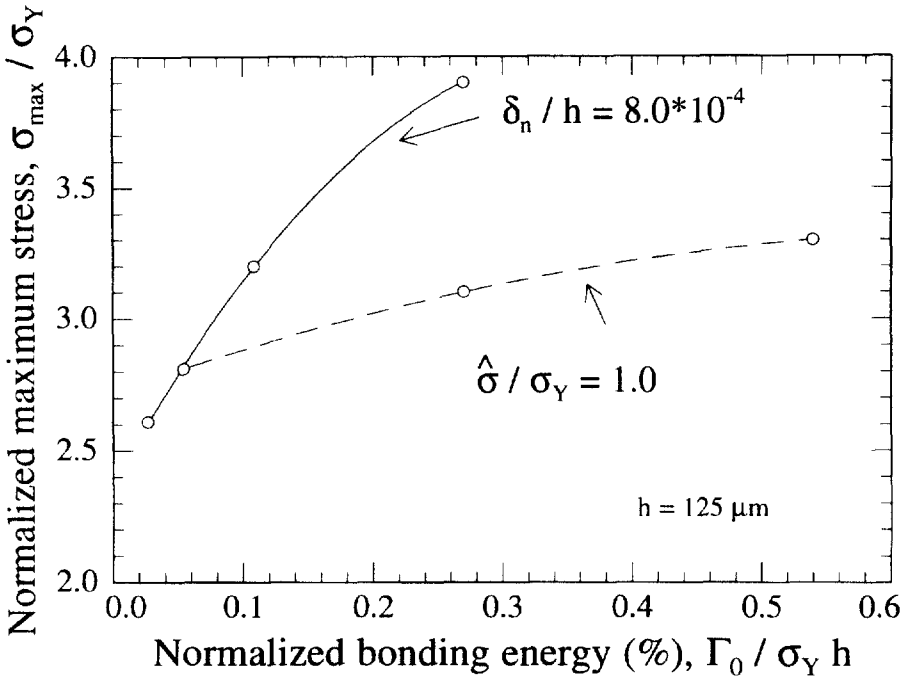

Fig. 19. Effect of bonding energy on the maximum nominal stress. The solid line (for constant δ_n, varying $\hat{\sigma}$) shows the variation of the maximum stress as a function of the peak interfacial stress, $\hat{\sigma}$ (note, $\Gamma_0 = 0.5\ \hat{\sigma}\delta_n\ (1+\lambda_2-\lambda_1)$). The dotted line (holding $\hat{\sigma}$ constant, varying δ_n) shows the variation of the maximum stress as a function of δ_n.

stresses. The role of the residual stresses is to increase the initial yield stress of nickel by about 20%. One may be tempted to conclude that it is simply this increase in the initial yield stress that leads to higher values of σ_{max} and hence to higher fracture toughness. To investigate this hypothesis, we performed another calculation with the initial yield stress (at room temperature) set 20% higher than σ_Y (In this calculation, steps 1 and 2 are omitted, i.e. no residual stress calculation). This result is also shown in Fig. 18. Figure 18 shows that the value of σ_{max} for this calculation is just slightly higher than the calculation with σ_Y as the initial yield stress (and without residual stresses) leading us to conclude that the factor 1.3 increase in σ_{max} is mainly due to the compressive preload on the cracks in the ceramic which must be first overcome before significant additional tensile loading of the metal strip occurs.

7. Conclusions

Figures 10 and 11 are re-plotted on a different scale in Fig. 19. This figure shows that the average maximum nominal stress is more sensitive to the changes in $\hat{\sigma}$ than to the changes in δ_n for the given value of bonding energy. It must be noted that for $\hat{\sigma}/\sigma_Y \geqslant 6$, the average nominal stress did not reach a plateau, and the interface is too strong to debond. Convergence of the finite element

simulation becomes a problem when δ_n was reduced by 10 times, indicating some correlation between the mesh resolution and this length scale.

Figures 14 and 15 imply that the interface parameters are $\hat{\sigma} = 1.8\,\sigma_Y = 148$ MPa; $\Gamma_0 = 11$ J m^{-2}, whereas the experimental investigations (Rose et al., 1983) on the atomic separation of two surfaces, have indicated that the bonding energy of separation of two surfaces is around 1 J m^{-2} and the cohesive strength is of the order of 10 σ_Y implying δ_n of the order of 1.0 nm. This is as expected and as pointed out by Tvergaard and Hutchinson (1993). Typically, the CCZ model should be viewed as a phenomenological and not as a model of atomic separation of two surfaces. Also, one may not expect continuum plasticity to work at the length scales of 1.0 nm which is far less than the dislocation spacing (≈ 1.0 μm) observed in metals. Because of the nonlinearity of the problem, no claim is made about the uniqueness of the parameters.

It may be concluded based on the present investigation that residual stresses induced by mismatch in the coefficients of thermal expansion have small effect on the debonding of the interface of platelets (away from the edges) during processing, however, they can significantly enhance the fracture toughness of a composite, in this case, by a factor of 1.3–1.6. The increase in the fracture toughness derives from the strain hardening of the metal strip, which in turn is encouraged due to compressive stresses developed in front of the debond crack as a result of residual stress field.

Our calculations show that maximum work of rupture can be achieved for the interfaces which are neither too strong nor too weak. Figure 20 shows estimated work of rupture as a function of

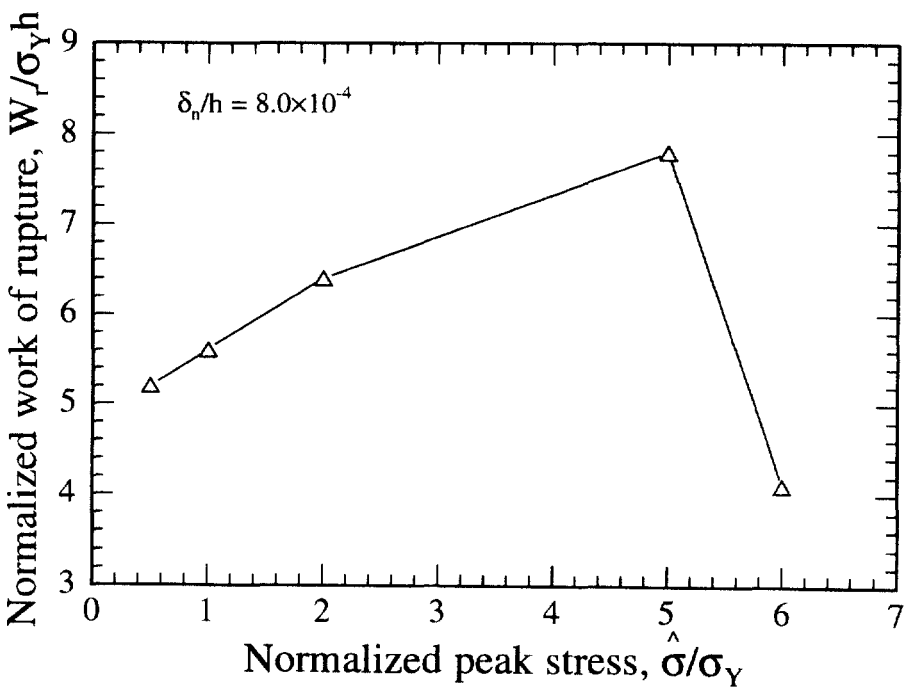

Fig. 20. Effect of the interfacial strength on the estimated work of rupture. Beyond $\hat{\sigma}/\sigma = 5$ debonding does not occur and the metal fails at a small value of crack opening displacement.

the interfacial strength, $\hat{\sigma}$, based on the analysis in Section 6.2. The maximum work of rupture is estimated to be $7.8\,\sigma_Y h$ for $\hat{\sigma}/\sigma_Y = 5.0$.

Acknowledgements

This research was supported by the Air Force Office of Scientific Research under contract F49620-931-0235, and by the Materials Science Center (MSC) at Cornell, supported by the National Science Foundation under awards DMR-9121654 and DMR-9632275. The computations were performed using the Central computing Facility maintained by the MSC. We thank HKS for permission to use ABAQUS under academic license. The first author would also like to thank Profs Sass and Dawson of Cornell University for their comments.

Appendix

Figure 21 shows a typical 4-noded interface element of length l_e. The normal and tangential vectors to the interface element are shown by **n** and **t**. Figure 21(b) shows the same interface element in the normalized coordinate, ξ, where

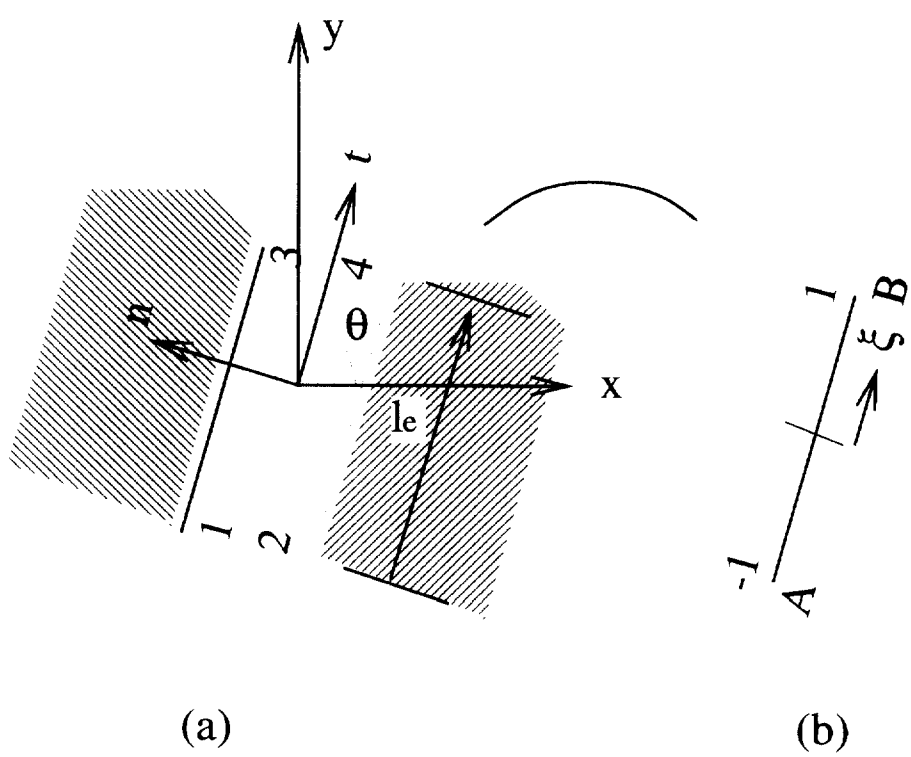

Fig. 21. Schematic of an interface element of length l_e. ξ represents the normalized coordinate along the length of element.

$$\xi = \frac{\sqrt{(x-x_A)^2+(y-y_A)^2}-\sqrt{(x-x_B)^2+(y-y_B)^2}}{l_e}$$

and x_A, y_A and x_B, y_B represent coordinates of nodes 1 (and 2) and 3 (and 4), respectively. In Fig. 21(b), point A represents nodes 1 and 2, and point B represents nodes 3 and 4. The displacements of a node, i, have two components

$$\mathbf{U}_i = \begin{pmatrix} U_{ix} \\ U_{iy} \end{pmatrix},$$

and the eight components of element displacements, $\mathbf{U}^e$, are listed as

$$\{U\} = [\mathbf{U}_1\, \mathbf{U}_2\, \mathbf{U}_3\, \mathbf{U}_4]^T.$$

Let

$$\Delta U_x^A = U_{1x} - U_{2x},$$

$$\Delta U_y^A = U_{1y} - U_{2y},$$

$$\Delta U_x^B = U_{3x} - U_{4x},$$

$$\Delta U_y^B = U_{3y} - U_{4y},$$

then one can write

$$\{\Delta U\} = [\Delta U_x^A\, \Delta U_y^A\, \Delta U_x^B\, \Delta U_y^B]^T \tag{9}$$

$$\{\Delta U\} = [\mathbf{H}]\{U\}, \quad \text{and} \tag{10}$$

$$[\mathbf{H}] = \begin{bmatrix} 1 & 0 & -1 & 0 & 0 & 0 & 0 & 0 \\ 0 & 1 & 0 & -1 & 0 & 0 & 0 & 0 \\ 0 & 0 & 0 & 0 & 1 & 0 & -1 & 0 \\ 0 & 0 & 0 & 0 & 0 & 1 & 0 & -1 \end{bmatrix}. \tag{11}$$

The displacements within an interface element are uniquely defined by the eight components of $\mathbf{U}^e$, or in other words, the separation of the interface within an element is uniquely defined by the vector $\Delta\mathbf{U}$. For a linearly varying field of displacements, $\Delta\mathbf{u}_{xy}$, one can write

$$\{\Delta u_{xy}\} = [\mathbf{N}]\{\Delta U\}, \tag{12}$$

where N_{ij} are the shape functions for the element. The elements of the matrix [N] in normalized coordinates are

$$[\mathbf{N}] = \begin{bmatrix} \frac{1}{2}(1-\xi) & 0 & \frac{1}{2}(1+\xi) & 0 \\ 0 & \frac{1}{2}(1-\xi) & 0 & \frac{1}{2}(1+\xi) \end{bmatrix}. \tag{13}$$

The interface constitutive law is

$$T_n = F(\lambda)\Delta\hat{u}_n$$

$$T_t = \frac{\delta_n}{\delta_t} F(\lambda) \Delta\hat{u}_t,$$

where $\Delta\hat{u}_n = \Delta u_n/\delta_n$ and $\Delta\hat{u}_t = \Delta u_t/\delta_t$ are the normalized normal and tangential interface separations, and $F(\lambda) = \sigma(\lambda)/\lambda$. also, recall

$$\lambda = (\{\Delta\hat{u}\}^T\{\Delta\hat{u}\})^{1/2}.$$

If the angle between the x-direction and the tangential direction of an interface element is θ, then one can write

$$\{\Delta u\} = [\Delta u_n \, \Delta u_t]^T,$$

$$\{\Delta u\} = [\Theta]\{\Delta u_{xy}\}, \quad \text{where}$$

$$[\Theta] = \begin{bmatrix} -\sin\theta & \cos\theta \\ \cos\theta & \sin\theta \end{bmatrix}. \tag{14}$$

Let

$$[\Delta] = \begin{bmatrix} \frac{1}{\delta_n} & 0 \\ 0 & \frac{1}{\delta_t} \end{bmatrix}, \tag{15}$$

$$\{t'\} = [t_n \, t_t]^T, \quad \text{and} \tag{16}$$

$$[\Sigma] = \begin{bmatrix} F(\lambda) & 0 \\ 0 & \frac{\delta_n}{\delta_t} F(\lambda) \end{bmatrix}, \tag{17}$$

then we can write the normalized displacements as

$$\Delta\hat{u} = \mathbf{\Delta\Theta NHU} = \hat{\mathbf{B}}\mathbf{U}, \tag{18}$$

where $\hat{\mathbf{B}} = \mathbf{\Delta\Theta NH}$. The interface law can be written in the matrix form as

$$\{t'\} = [\Sigma][\Delta]\{\Delta u\}, \quad \text{or}$$

$$\{t'\} = [\Sigma][\Delta][\Theta][N][H]\{U\}. \tag{19}$$

References

Allen, D.H., Jones, R.H., Boyd, J.G., 1994. Micromechanical analysis of a continuous fiber metal matrix composite including the effects of matrix viscoplasticity and evolving damage. J. Mech. Phys. Solids 42, 505–529.

Ashby, M.F., Blunt, F.J., Bannister, M., 1989. Flow characteristics of highly constrained metal wires. Acta Metall. 37, 1847–1857.

Bannister, M., Ashby, M.F., 1991. The deformation and fracture of constrained metal sheets. Acta Metall. Mater. 39, 2575–2582.

Bao, G., Hui, C.-Y., 1989. Effects of interface debonding on the toughness of ductile particle reinforced ceramics. Int. J. Solids Structures 22, 325–348.

Barenblatt, G.I., 1962. Mathematical theory of equilibrium cracks. Adv. Appl. Mech. 7, 56–129.

Bose, K., Ponte Castaneda, P., 1992. Stable crack growth under mixed-mode conditions. J. Mech. Phys. Solids 40, 1053–1103.

Budiansky, B., Hutchinson, J.W., Lambropoulos, J.C., 1983. Continuum theory of dilatant transformation toughening in ceramics. Int. J. Solids Structures 19, 337–355.

Budiansky, B., 1986. Micromechanics II. Proceedings of Tenth U.S. Congress on Applied Mechanics, pp. 25–32.

Dugdale, D.S., 1960. Yielding of steel sheets containing slits. J. Mech. Phys. Solids 8, 100–104.

Hutchinson, J.W., 1987. Crack tip shielding by micro-cracking in brittle solids. Acta Metall. 35, 1605–1609.

Kolhe, R., Hui, C.Y., Ustundag, E., Sass, S.L., 1996. Residual thermal stresses and calculation of the critical metal particle size for interfacial crack extension in metal-ceramic matrix composites. Acta Metall. 44, 279–287.

Kolhe, R.B., 1997. Fracture toughness and metal-ceramic-matrix composites. PhD. thesis, Cornell University.

Mataga, P.A., 1989. Deformation of crack-bridging ductile reinforcements in toughened brittle materials. Acta Metall 37, 3349–3359.

McMeeking, R.M., Evans, A.G., 1982. Mechanics of transformation-toughening in brittle materials. J. Am. Ceram. Soc. 65, 242–246.

Needleman, A., 1987. A continuum model for void nucleation by inclusion debonding. J. Appl. Mech. 54, 525–531.

Needleman, A., 1990. An analysis of tensile decohesion along an interface. J. Mech. Phys. Solids 38, 289–324.

Rodeghiero, E.D., Ustundag, E., Wuthenow, M., Sass, S.L., Giannelis, E.P., 1996. The nature of ductile phase toughening in Ni/α–Al_2O_3 metal-ceramic composites. Ceramic Trans., Adv. in Ceramic-matrix Composites III 74, 353–364.

Rose, J.H., Smith, J.R., Ferrante, J., 1983. Universal features of bonding in metals. Phys. Rev. B 28, 1835–1845.

Sharma, S.M., Aravas, N., 1993. On the development of variable-separable asymptotic elastoplastic solutions for the interface cracks. Int. J. Solids Structures 30, 695–723.

Sigl, L.S., Mataga, P.A., Dalgleish, B.J., McMeeking, R.M., Evans, A.G., 1988. On the toughness of brittle materials reinforced with ductile phase. Acta Metall. 36, 945–953.

Thurston, M., 1994. Influence of Residual Stresses on Ceramic-Metal Interfacial Toughness. PhD. thesis, Cornell University.

Thurston, M., Zehnder, A.T., 1996. Nickel–alumina interfacial fracture toughness: experiments and analysis of residual stress effects. Int. J. of Fract. 76, 221–241.

Tuan, W.H., Brook, R.J., 1990. The toughening of alumina with nickel inclusions. J. Eur. Ceram. Soc. 6, 31–37.

Tvergaard, V., 1990. Effect of fiber debonding in a whisker-reinforced metal. Mater. Sci. Engng. 203–213.

Tvergaard, V., 1991. Effect of thermally induced residual stresses on the failure of a whisker-reinforced metal. Mech. Mater. 11, 149–161.

Tvergaard, V., 1992. Effect of ductile particle debonding during crack bridging in ceramic. Int. J. Mech. Sci. 34, 635–649.

Tvergaard, V., Hutchinson, J.W., 1992. The relation between crack growth resistance and fracture process parameters in elastic-plastic solids. J. Mech. Phys. Solids 40, 1377–1397.

Tvergaard, V., Hutchinson, J.W., 1993. The influence of plasticity on mixed mode interface toughness. J. Mech. Phys. Solids 41, 1119–1135.

Tvergaard, V., Hutchinson, J.W., 1994a. Toughness of an interface along a thin ductile layer joining elastic solids. Phil. Mag. A 70, 641–656.

Tvergaard, V., Hutchinson, J.W., 1994b. Effect of t-stress on mode I crack growth resistance in a ductile solid. Int. J. Solids Structures 31, 823–833.

Tvergaard, T., Hutchinson, J.W., 1996a. On the toughness of ductile adhesive joints. J. Mech. Phys. Solids 44, 789–800.

Tvergaard, V., Hutchinson, J.W., 1996b. Effect of strain dependant cohesive zone model on predictions of crack growth resistance. Int. J. Solids Structures 33, 3297–3308.